A new constraint on the central Andean rotation pattern from paleomagnetic studies in the southern Subandes of Bolivia

Juan M. Calvagno, Leandro C. Gallo, Renata N. Tomezzoli, Ernesto O. Cristallini, Alejandra Dalenz Farjat, Roberto M. Hernández

PII: S0895-9811(19)30453-5

DOI: https://doi.org/10.1016/j.jsames.2019.102470

Reference: SAMES 102470

To appear in: *Journal of South American Earth Sciences*

Received Date: 27 August 2019

Revised Date: 13 December 2019

Accepted Date: 13 December 2019

A new constraint on the central Andean rotation pattern from paleomagnetic studies in the southern Subandes of Bolivia

Juan M. Calvagno[1,2], Leandro C. Gallo[1,2], Renata N. Tomezzoli[1,2], Ernesto O. Cristallini[1,3,4], Alejandra Dalenz Farjat[5], Roberto M. Hernández[4,5]

[1]*Consejo Nacional de Investigaciones Científicas y Técnicas (CONICET), Universidad de Buenos Aires. Departamento de Ciencias Geológicas, Facultad de Ciencias Exactas y Naturales, Ciudad Universitaria, Pabellón II C1428EH, Buenos Aires, Argentina.*

E-mail:juanmacalvagno@gmail.com

[2]*Instituto de Geociencias Básicas, Aplicadas y Ambientales de Buenos Aires (IGEBA),*

[3]*Laboratorio de Modelado Geológico (La.Mo.Ge.), Instituto de Estudios Andinos (IDEAN).*

[4]*Laboratorio de Termocronología (La.Te Andes-CONICET), Consejo Nacional de Investigaciones Científicas y Técnicas, Salta, Las Moreras 310, A4401XBA, Vaqueros, Salta.*

[5] *XR-GEOMAP. Avenida Ricardo Durand 397. Salta*

Keywords: Anisotropy of Magnetic susceptibility; Paleomagnetism; Rock magnetism; Central Andean Rotation Pattern

Abstract

New paleomagnetic and anisotropy of magnetic susceptibility (AMS) studies were performed in the southern Subandes of Bolivia in order to assess vertical axis rotations in a poorly studied area. Due to the presence of polarity reversals, it was possible to perform a reversal test that provided evidence of a reliable paleomagnetic record interpreted to be primary. In an area where vertical axis rotations are a principal component of deformation, we have developed a nonparametric method for the determination of tectonic rotations. We calculated a paleomagnetic pole for the Miocene Tariquia Formation (Lat.= 78.4º S, Long.= 113.1º E, A95= 3.5º, N= 72, K= 23.73, Slat= 22.08º, SLon= 64.06º) and from our results, rotations around vertical axes, commonly sought around the Arica-Santa Cruz bend were ruled out. From the integration of paleomagnetic and AMS results, it was seen that the magnetic lineation lies within the bedding plane, consistent with the early stages of layer parallel shortening. However, it is not parallel to the structural trend, implying material displacement parallel to it. In concomitance with paleomagnetic results, this allows us to argue that a local change in the azimuth of the structures at this latitude could be the consequence of an asymmetric or heterogeneous basement and/or exogenous agents like differences in erosion along the course of the structures during the evolution of the Bolivian fold and thrust belt.

1 Introduction

Throughout the entire South American west margin, a first order tectonic feature is the prominent bend in both the continental margin and the orogenic system near 20ºS - also known as the Bolivian orocline (Carey, 1955). The Central Andes at this latitude can be subdivided into five main physiographic units (from west to east): Western Cordillera, Altiplano-Puna plateau, Eastern Cordillera, inter-Andean zone, and Subandean ranges. The Subandean ranges are a thin-skinned fold and thrust belt characterized by narrow NNE elongated anticlines separated by syncline valleys, forming continuous and parallel belts (Fig. 1, Belotti et al., 1995). The southern Subandes of Bolivia are separated from the Puna-Altiplano system by the Eastern Cordillera, which transferred eastward thrusting to this tectonic province at the end of the Miocene (Eichelberger et al., 2013; Lease et al., 2016; Uba et al., 2009). Thus, the Subandean ranges accommodated the most recent phase of deformation from ca. 15 Ma and, actively deforming today, the wedge front is currently being propagated there (Brooks et al., 2011).

Carey (1955) coined the term “Bolivian orocline” and proposed that the curvature is the result of a secondary bending of an originally straight orogenic belt. Later, Isacks (1988) hypothesized that this feature was the result of along strike differential Neogene horizontal shortening, with maximum shortening estimates occurring near the axis of the bend, decreasing northward to Peru and southward toward Argentina (Fig. 1). These changes would need to be accompanied by tectonic rotations around vertical axis in the fore arc. However, the required horizontal shortening gradient between the core and the limbs is not supported by recent shortening estimates (Kley, 1996; McQuarrie, 2002; McQuarrie et al., 2008).

Our understanding of the spatial distribution and timing of deformation have improved in recent years, and paleomagnetic data throughout the entire orogenic system (e.g. Arriagada et al., 2006; Barke et al., 2007; Roperch et al., 2006; Somoza et al., 1996, 2015; Somoza and Tomlinson, 2002) currently resolve, at the regional scale, the so-called central Andean rotation pattern (CARP), defined by Somoza et al. (1996). This data defines a broad rotation pattern of clockwise rotations in the southern limb and counterclockwise rotations in the northern limb, which is coincident with present geodetic observations (Allmendinger et al., 2005). This pattern suggests that small-block rotations driven by distributed shearing of the Central Andean crust are the dominant process related to the curvature of the Central Andes (e.g. Arriagada et al., 2008; Eichelberger et al., 2013; Somoza and Tomlinson, 2002). But orogenic curvature is best classified based on kinematic history (see Weil and Sussman, 2004, and references therein), which requires combining bulk shortening and vertical axis rotations with finite strain directional data (e.g. Eichelberger and McQuarrie, 2014; Weil et al., 2010). Recent studies based on this data, classify the Bolivian orocline as a progressive arc that develops increasing structural curvature and vertical axis rotation during deformation. Moreover, the curvature has been developing as a consequence of curved deformation paths (e.g. Arriagada et al., 2008b; Eichelberger et al., 2013) implying 3-D kinematics and the necessity of accounting for material displacement parallel to the orogenic belt, that is not addressed in 2-D cross sections. Thus, an understanding of the orientation of shortening is key for defining the kinematic evolution of the Bolivia orocline, here addressed by anisotropy of magnetic susceptibility (AMS).

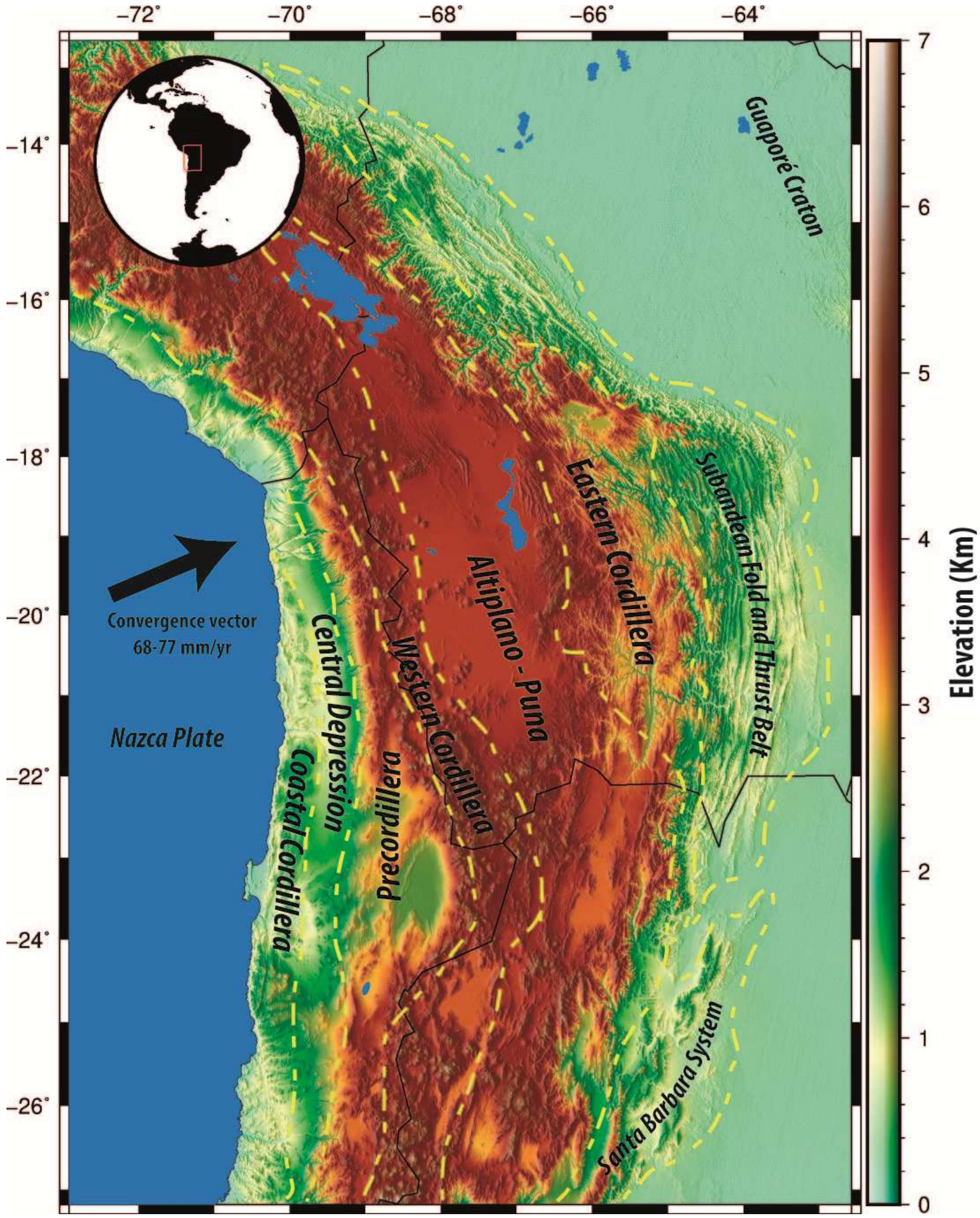

Figure 1. Digital elevation model of the Central Andes. Dashed lines represent the approximate boundaries of the main morphotectonics units.

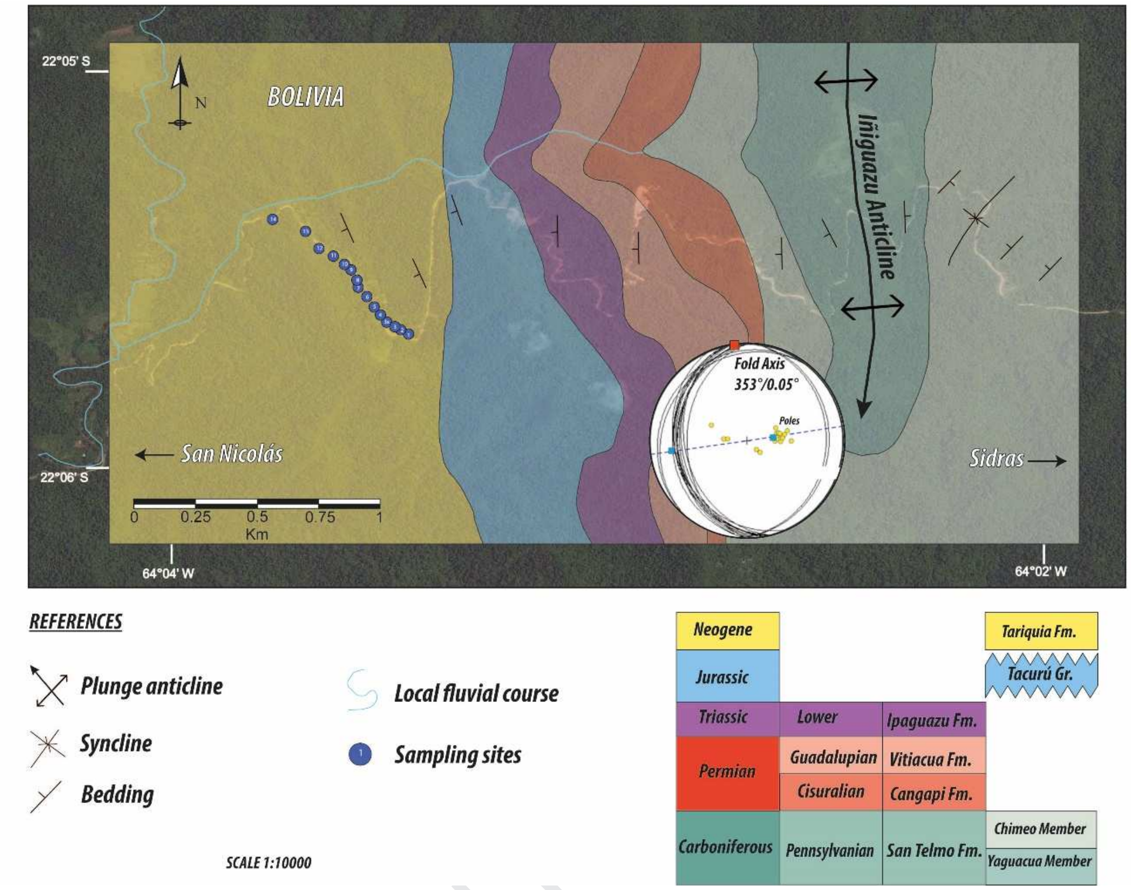

Figure 2. Geological map of the Iñiguazu anticline and surrounding areas with the location of the paleomagnetic sites sampled. Stereographic projection shows the bedding planes with their respective poles, and the main trend of the anticline (NNW).

This study presents new paleomagnetic data from Miocene deposits from the Iñiguazu anticline, located in the southern Subandean ranges of Bolivia to assess vertical axis rotations in a poorly studied area. Moreover, through the use of anisotropy of magnetic susceptibility (AMS), we assess the direction of shortening and the contribution of layer parallel shortening (LPS) in the total shortening budget.

2 Geological framework

Subduction of the oceanic Nazca plate beneath South America has driven deformation and magmatism from late Cretaceous heretofore (Somoza and Zaffarana, 2008), leading the tectonic uplift of the Central Andes and coupled subsidence of sedimentary basins along this convergent plate boundary. Andean foreland basin systems contain long-lived successions recording the timing of exhumation and deformation, thus providing key records to unravel the patterns of Andean mountain building.

In particular, the Subandean foreland basin registers the growth of the orogeny since 20 My and its interaction with the advancing central Andean fold-thrust belt (e.g. Uba et al., 2009, 2005). This greater than 10 km thick foreland succession is composed of Oligocene to Quaternary clastic deposits that disconformably overlie Jurassic–Cretaceous Ichoa Formation aeolian sandstones. Although the exact age and distribution of sedimentary facies vary within the basin as a function of timing of deformation and coupled flexural subsidence, previous studies have recognized several equivalent lithostratigraphic units throughout the entire basin (Calle et al., 2018; Uba et al., 2005). The main body of sedimentation of this foreland sedimentation represents mixed anastomosing and braided fluvial systems defined by the upper Miocene sandstones and mudstones of the Tariquia Formation. This study explores the foreland sedimentation of the Tariquia Formation outcropping at the Iñiguazú anticline at 22ºS.

3. Stratigraphy and structure

3.1 Stratigraphy

In this contribution, the Miocene deposits of Tariquia Formation that overly Jurassic-Cretaceous eolian quartzite sandstones were sampled (Fig. 3). Calle *et al* (2018) from sedimentology and U-Pb geochronology interpret this section of the Subandean foreland systems with an early-middle Miocene (~24-12 Ma) age.

The sequence is composed of 60 meters of lenticular banks of medium to fine purple to brown colored sandstones, with intraclasts of pellets at the base of the banks and tractive structures, such as ripples and/or cross bedding stratification (Fig. 3). 1 to 5 meters thick sandstone beds are interspersed with smaller banks (0.5 to 2 m) of reddish siltstones and claystones with parallel lamination. The sandstone beds have erosive and net contacts at the base and are mostly amalgamated. The depositional environment was interpreted as a braided river.

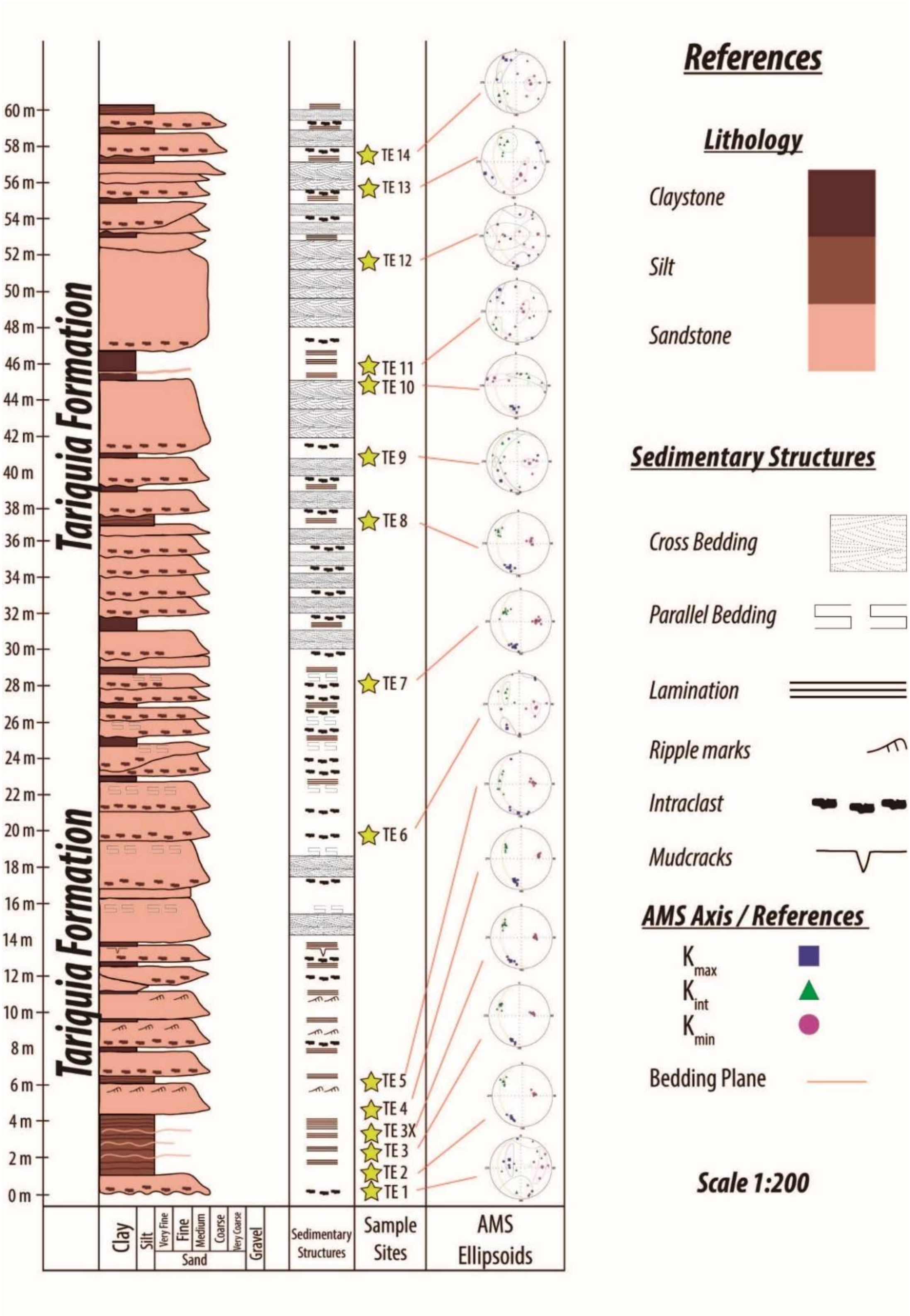

Figure 3. Tertiary stratigraphic sequence outcropping in the western limb of the Iñiguazu anticline in the Subandean Ranges. The sequence is composed of lenticular banks of medium to fine purple to brown colored sandstones, with intraclasts of pellets at the base of the banks and tractive structures.

The depositional environment was interpreted as a braided river. Paleomagnetic site positions with the respective AMS stereonets are indicated.

3.2 Structure

The Iñiguazu anticline (S 22º 05', W 64º 04') is a symmetric structure with oriental vergence. The dip of the fold axis is less than 5° (Fig. 2). The attitude of the bedding planes is NNW-SSE (168° on average, Fig. 4b) and inclinations between 25° and 40° to the west (bedding strike 0º-360º and dip 90° clockwise from given strike, 0º-90º).

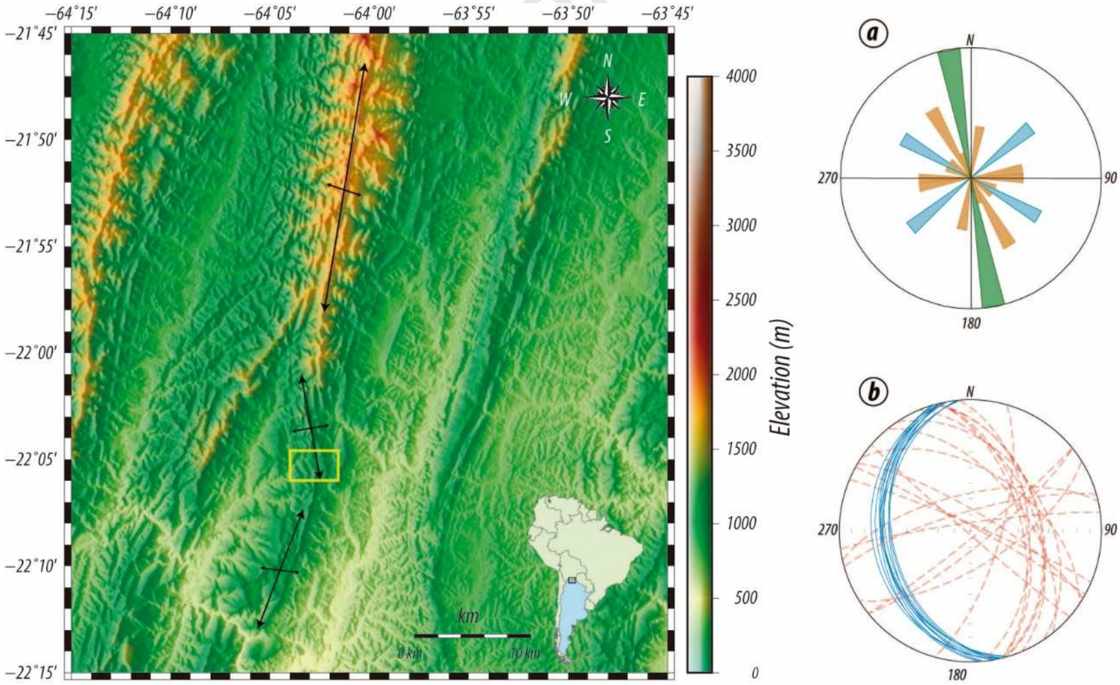

Figure 4. Structure features and digital elevation model of the Iñiguazu anticline. The yellow square shows the work area. The azimuth of the structure in this area (NNW-SSE) differs from the general azimuth of the entire anticline (NNE-SSW). At least three patterns of joints have been identified. **(a)** The most predominant is parallel to the axis of

the fold (green), and the other two correspond to oblique (orange) and perpendicular (blue) of it. **(b)** Ciclographics (red) of the fractures and their relations with the bedding planes (blue). They tend to be orthogonal to the layers of the *in situ* stratification, implying that they have been developed during the initial stages of the deformation.

From the measurement of the joints in the Neogene layers (Fig. 4a), it arises that there are three different populations. There is a predominant population parallel to the axis of the fold where the curvature is maximum (Twiss and Moores, 1992; Fig. 4a, green color). The remaining two populations correspond to oblique and perpendicular fractures to the fold axis. It appears that they tend to be orthogonal to the stratification *in situ* (Fig. 4b). This suggests that they have begun to be developed during the initial stages of deformation (i.e. layer parallel shortening) and so the directional analysis should be done by previously restoring the structure. The directional disposition of the fractures (Fig. 4a) presents certain symmetry, with the main axis NNW-SSE consistent with the local azimuth of the layers (NNW-SSE), but not with the regional direction of the Iñiguazu anticline (NNE-SSW) (Fig. 4).

4 Methodologies

4.1 Sampling

Ninety-nine (99) specimens were taken for paleomagnetic and anisotropy of magnetic susceptibility (AMS) studies. They were distributed vertically along to the stratigraphic profile in fifteen sites (TE1 to TE14 and TE3X) with 5 to 7 specimens per site. The specimens were collected with a portable gasoline-powered drill and oriented in the field using magnetic and sun compasses and inclinometer; no differences were found between both readings.

4.2 Techniques

Room temperature anisotropy of magnetic susceptibility (RT-AMS) was measured before the paleomagnetic study to shed light on the relationship between the magnetic fabric of the rocks and the evolution of the structure. RT-AMS was measured with an MFK-1A Kappabridge (AGICO).

The basis of the method is the application of a low-intensity magnetic field in 15 different positions, with the objective of defines how the induced magnetization is oriented due to the internal anisotropies of the samples. The results were analyzed with the Anisoft 42® software to obtain directional results and AMS scalar axes represented in the ellipsoids and their statistic parameters, in situ and with bedding correction, also the anisotropy degree (P*j*) values and shape parameter (T) (Jelinek 1981; Table 1).

Paleomagnetic measurements were made using a 2G DC-squid cryogenic magnetometer at the University of Buenos Aires. Thermal demagnetization proved to be more effective for the isolation and determination of the magnetic components. Hence, the whole collection of samples was submitted to thermal cleaning in at least 13 steps, with maximum temperatures of 580 °C to 680 °C, with successive increments of 100º, 50º and 25ºC, in a dual chamber TD-48 ASC paleomagnetic furnace. Bulk susceptibility of the samples was measured after each step to analyze possible mineralogical changes during heating, with a Bartington MS2 susceptibility meter.

Demagnetization results were analyzed using orthogonal vector plots (Zijderveld, 1967) and stereographic projections. Paleomagnetic directions were determined using principal component analysis (PCA) from at least four successive steps (Kirschvink, 1980).

A subset of representative samples was further studied to characterize their magnetic mineralogy. Thermomagnetic analysis (χ–T) was carried out using an AGICO MFK1-FA with an alternating field of 200 A/m and a frequency of 976 Hz, equipped with a CS-4 temperature control system. Furthermore, the isothermal remanent magnetization (IRM) was induced using an ASC Model IM-10-30 Impulse Magnetizer successively with pulsed fields of 5 T. The IRM was measured using an AGICO JR-6A Dual Speed Spinner Magnetometer.

5 Results

5.1 Rock Magnetism

Eight samples along the profile were selected for low-temperature and high-temperature susceptibility experiments. All of the low-temperature thermomagnetic curves (k *vs* t) are a hyperbola (Fig. 5), representing paramagnetic minerals (Hrouda et al., 1997).

From the comparison of the shape of the heating and cooling curves, it can be inferred due to the irreversibility of the curves, and a Hopkinson peak (Dunlop and Özdemir, 1997) at 500ºC (Fig. 5), possible structural chemical transformations. Plus, low values of susceptibility allow to infer the presence of titanohematite due to the replacement of small amount of iron per titanium. In this way, the titanohematite can conserve the magnetic properties of hematite but the Curie temperature descends to ~500ºC (Dunlop & Özdemir 1997).

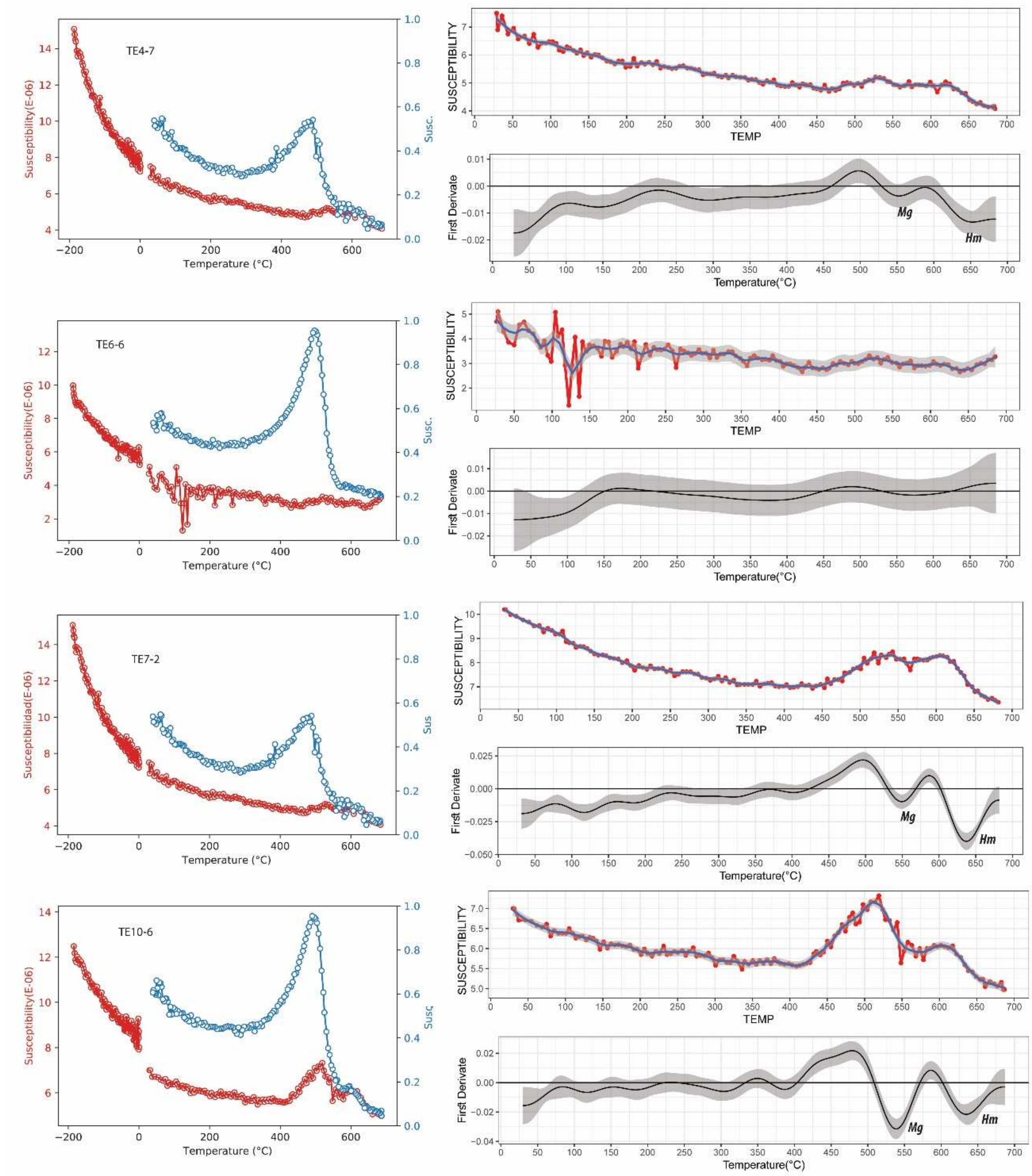

Figure 5. Left column shows the representative low and high thermomagnetic curves (k vs t). Red lines correspond to heating curves; blue lines correspond to cooling curves. Note that the thermomagnetic curves show hyperbolic behavior, indicating the presence of paramagnetic minerals and the Hopkinson peak around 500ºC. Due to the irreversibility of the curves, it is not ruled out a possible structural chemical transformation. Low values of susceptibility allow inferring the presence of titanohematite due to the replacement of a small amount of iron per titanium. The right

column shows the spline fitting of the heating curve and its first derivate indicating Curie/Neel temperatures of representative magnetic mineralogy.

Coercivity components and IRM acquisition curves were performed (Fig. 6). Due to the antiferromagnetic behavior found during the AF demagnetization, the study was done with a 5 T coil. The entirety of the samples did not reach the saturation in the presence of pulsed DC fields up to 3 T. This behavior shows that the magnetization is not carried by ferromagnetic minerals; particularly there is no evidence of the presence of magnetite in the samples in accordance with NRM magnetization and thermomagnetic curves.

Modeling of coercivity spectra was performed using a fitting program (Maxbauer et al., 2016). The model was fitted using two possible components, both with high coercivity. The lack of saturation of the samples and the high coercivity of the present minerals show that the magnetization is carried probably by non-stoichiometric hematite.

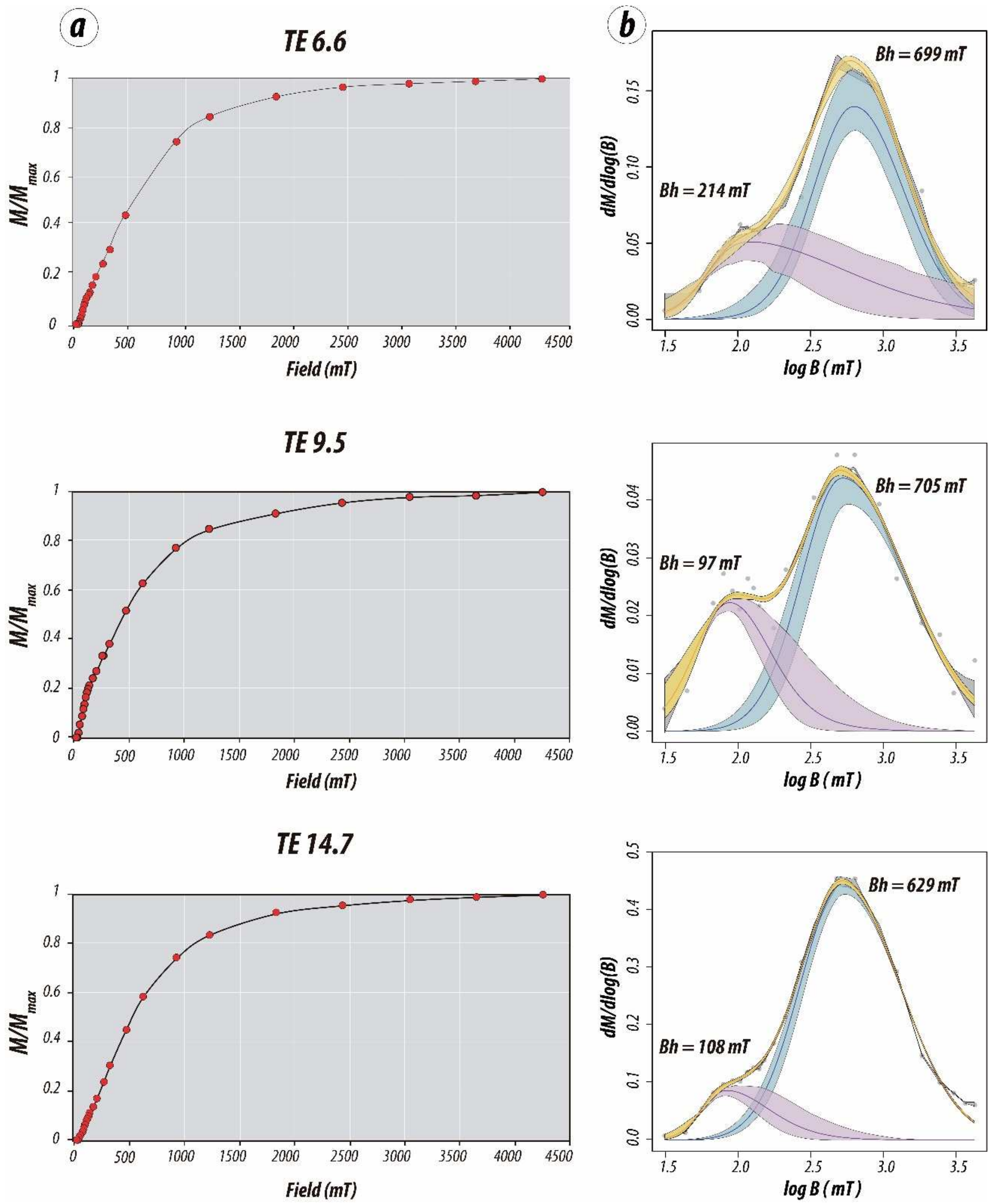

Figure 6. (a) Normalized acquisition curves of isothermal remanence magnetization (IRM) (b) Model coercivity spectra of selected samples. Data points are denoted by dots. The blue line represents the high coercivity component and the purple line represents the low coercivity component. Blue and purple shadows represent 95% confidence intervals.

5.2 Anisotropy of Magnetic Susceptibility (AMS)

The results of each of the 15 sites studied show internal statistical consistency. Most of the sites have oblate to triaxial fabric (Table 1), T> 0. The AMS K_{max} axes tend to be grouped towards the SW with an azimuth/inclination around 200° / 18°, this magnetic lineation is contained in the bedding planes. The K_{min} axes tend to be parallel to the stratification planes poles (Fig. 7; Table 1), in accordance with the early stages of layer parallel shortening (LPS; Weil and Yonkee, 2009).

The average susceptibility of the samples from the sites is $<21\times10^{-5}$ SI (Table 1, Fig. 8) suggesting that the AMS is mainly controlled by the orientation of the paramagnetic minerals within the crystalline structure (Tarling and Hrouda, 1993). From the discrimination of susceptibility by lithology, it is observed that every lithology has a characteristic susceptibility (Fig. 8c) but no functional relationship is found between P_j/T and susceptibility (Fig. 8d and e). This allows us to argue that the scalar parameters of AMS are mainly controlled by the stratigraphic position.

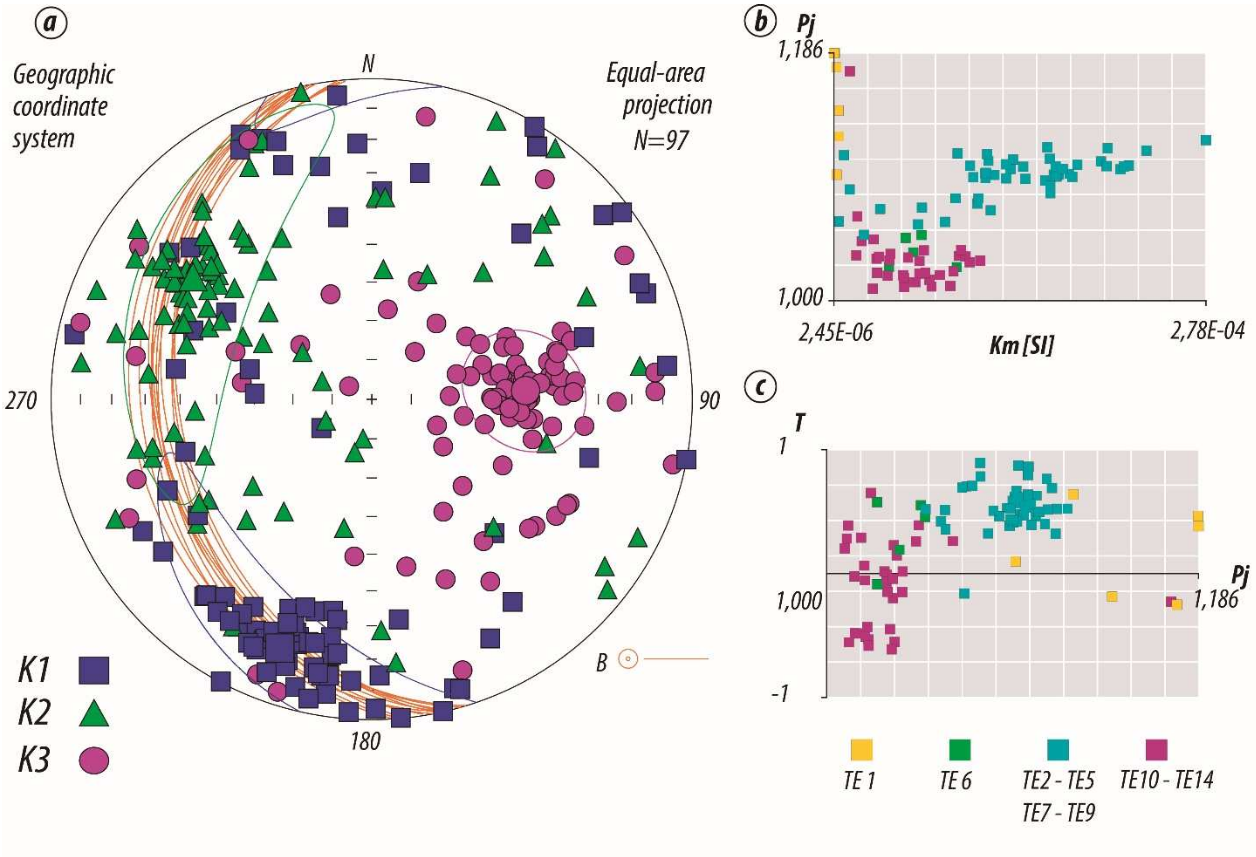

Figure 7. (a) Representation of the AMS ellipsoid axes *in situ* for the sampling location with their respective stratification planes (Orange lines, B) represented in an equal area projection in the Southern Hemisphere. The axes are maximum, intermediate and minimum, orthogonal to each other. **(b)** Mean susceptibility (Km) vs. anisotropy degree (Pj). There is a difference in the behavior of those sites located in the base, which present oblate ellipsoids with the highest Pj values (TE2-5 and TE7-9; light blue) with respect to those located to the top (TE10-14; bordeaux) with lower values of Pj and oblate and prolate type of ellipsoids. The TE1 (yellow) and TE6 (green) site behaviors differ from their stratigraphic neighbors' stand out. **(c)** Flinn graphs show the relationship between the shape parameter (T) vs the anisotropy degree (Pj) according to Jelinek (Jelinek, 1981). The anisotropy degree is <1.19.

From the scalar analysis of the AMS parameters, differences arise between the sites of the base with those of the top of the sequence (Fig. 8). The anisotropy degree (Pj) of the studied sequence is less than 1.19, increasing towards the base (TE1-5 and TE7-9, Table 1, Figures 7 and 8). The shape parameter T also changes from oblate to the base to prolate/oblate towards the top (TE11-12 and TE14; Figures 7 and 8; Table 1). The behavior of samples of the sites TE1 and TE6 differs from that of their stratigraphic neighbors. TE1 presents oblate and prolate ellipsoids and in TE6 the anisotropy degree is low. In both sites, the grain size corresponds to sandstones.

When the structural correction is applied on the AMS axes (i.e. each ellipsoid is corrected by taking the stratification plane to the horizontal), it is observed that the K*min* tend to be close to the vertical slightly imbricate to the southeast, and the K*max* tend to be aligned in an approximate NNE-SSW direction closed to the horizontal.

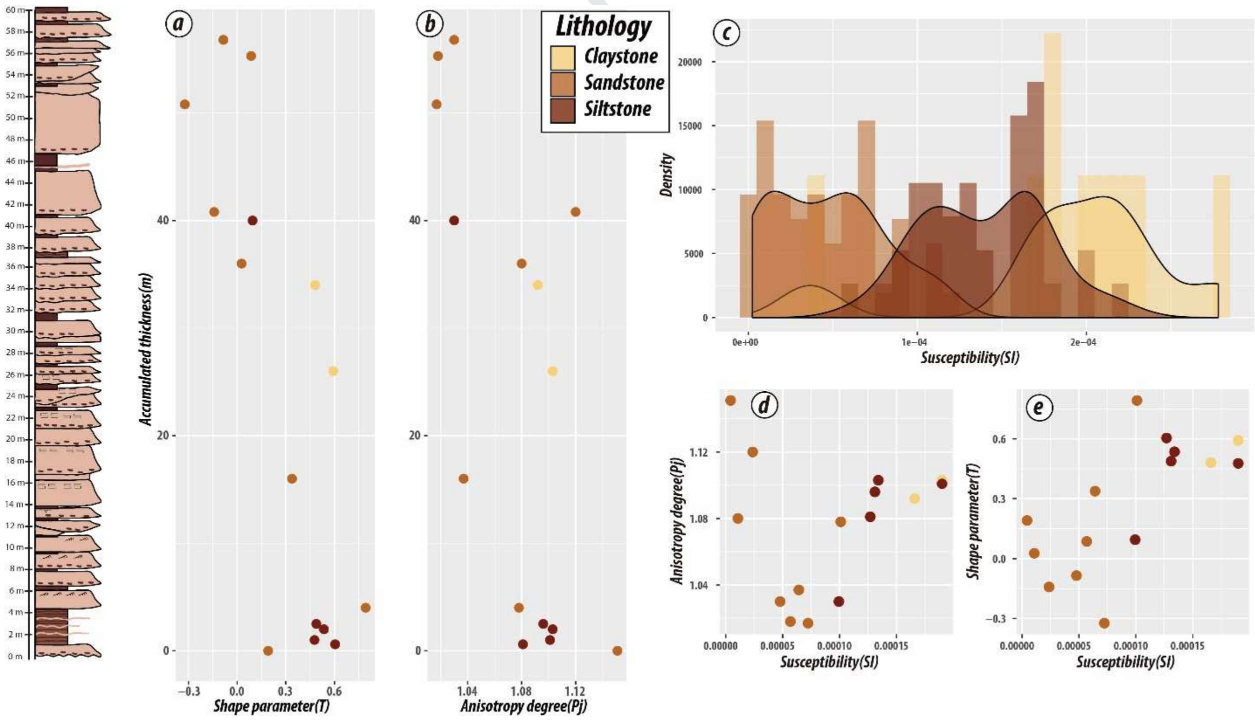

Figure 8. (a) Shape parameter (T), **(b)** Anisotropy degree (P_j) vs accumulated thickness. The shape parameter T changes from oblate at the base to prolate/oblate towards the top. The anisotropy degree P_j of the whole package is less than 19%, increasing towards the base. The average

susceptibility of the sites is <21x10-5 SI, suggesting that the anisotropy is mainly controlled by the orientation of the paramagnetic minerals within the crystalline structure. **(c)** Histogram showing the frequency of three different lithologies. Note that no strong functional relationship between anisotropy degree **(d)** or shape parameter **(e)** and magnetic susceptibility is seen, the scalar parameters of AMS are mainly controlled by the stratigraphic position.

Table 1. Anisotropy of magnetic susceptibility parameters. N/n: number of specimens measured/used in the calculation of the mean; L: lineation; F: magnetic foliation; Pj and T: anisotropy degree and shape parameter calculated according to the Jelinek (1981) statistics (See figures 7 and 8).

		Anisotropy of Magnetic Susceptibility Parameters						***Medias Eigenvectors***	
Site	**N/n**	K_{mean}	**Bedding Plane**	**L**	**F**	**Pj**	**T**	K_{max}	K_{min}
		(x10-5) SI	***Dec(°)/Inc(°)***	***K1/K2***	***K2/K3***			***Dec(°)/Inc(°)***	***Dec(°)/Inc(°)***
TE1	6/6	0,43	167/26	1,058	1,085	1,151	0,191	306/52	087/31
TE2	6/5	14,0	167/26	1,015	1,061	1,081	0,604	206/21	080/57
TE3	6/6	19,00	167/33	1,025	1,070	1,101	0,477	197/18	081/53
TE3X	7/7	13,40	164/34	1,022	1,074	1,103	0,535	204/19	088/53
TE4	8/8	13,10	168/39	1,023	1,068	1,096	0,488	195/25	080/41
TE5	7/6	10,20	163/33	1,008	1,068	1,084	0,788	354/01	085/56
TE6	5/5	6,42	166/36	1,011	1,024	1,037	0,338	207/14	103/44
TE7	9/8	21,00	175/34	1,019	1,076	1,103	0,592	195/16	088/45

TE8	5/5	16,60	176/32	1,022	1,065	1,092	0,481	200/18	079/57
TE9	7/5	1,32	169/29	1,036	1,039	1,080	0,027	220/19	099/57
TE10	6/5	10,00	170/34	1,014	1,016	1,030	0,095	185/27	290/27
TE11	7/5	2,23	170/34	1,075	1,036	1,120	-0,142	322/11	092/73
TE12	6/5	7,30	167/40	1,012	1,005	1,017	-0,323	176/02	085/27
TE13	6/5	5,67	168/39	1,008	1,009	1,018	0,086	248/06	150/52
TE14	8/5	4,00	174/38	1,016	1,013	1,030	-0,085	336/22	096/50

5.3 Paleomagnetic results

Most of the samples exhibit similar behavior, with a slight decay in their magnetization during the initial stages of heating until showing a more abrupt fall between 600ºC and 680ºC to the origin (Sites 1-8; 14, Fig. 9 and 10). Other samples exhibit an unstable and quasi-random behavior, with slight ascents and descents in their magnetization until their total or partial decay between 600ºC and 680ºC (sites 9-13). The blocking temperatures between 625ºC and 680ºC, as well as its continuous descent of the magnetization, show that the magnetization would be carried by hematite or titanohematite.

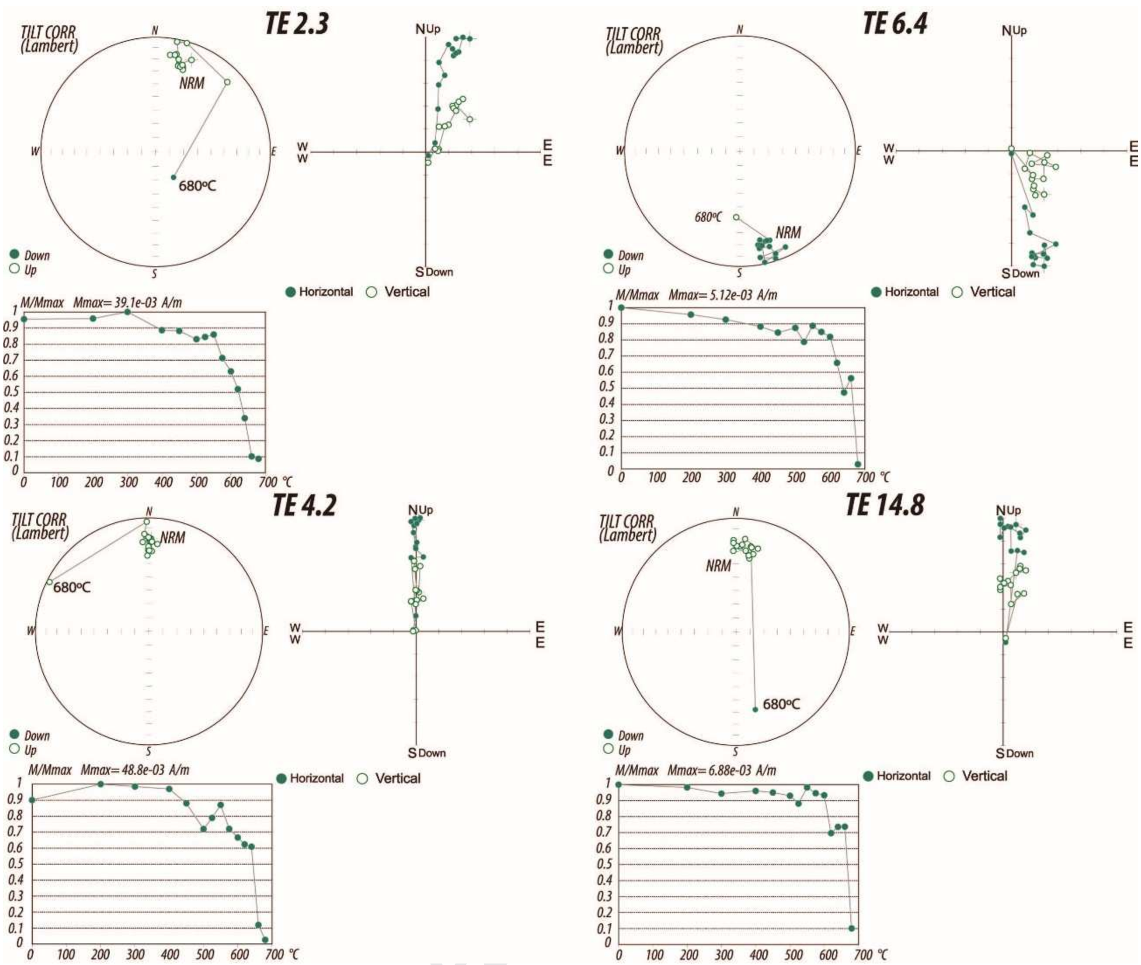

Figure 9. Representative thermal demagnetization behavior of different specimens after bedding correction. Zijderveld diagrams: open (filled) circles indicate vertical (horizontal) plane projections, in geographic coordinates; demagnetization curves; equal-area stereographic projection. See also Table 2.

Throughout the analyzed profile, there are normal and reverse polarities alternately. The isolated components corresponding to sites 1 and 6 are reversed while the components of sites 2 to 8 and 14 are normal (Table 2). Sites 9 to 13 do not have a well-defined polarity that can be indistinctly either normal or reverse. This variation could be due to oscillations and instabilities of the magnetic field during the reversals (e.g. Valet *et al.* 2016), or be the consequence that some of the lithologies are not suitable magnetic records.

269

Table 2. High-temperature characteristic remanent magnetization (ChRM) directions of the specimen in the Iñiguazu Anticline. Dec.: declination (º); Inc.: inclination (º); BP: bedding plane, strike and dip (90º clockwise from given strike); MAD (º): maximum angle deviation; k: Fisher statistical parameter (Fisher, 1953); n: number of specimens used in the calculation of the mean. The mean was calculated with the directions as reverse.

Specimen	Decº	Incº	BPº	Decº	Incº	MAD	Platº	Plongº	Polarity
	In Situ			*With bedding correction*					
TE12	334.8	1.5	167/26	155.4	4.0	6.3	-58.83	62.51	R
TE13a	160.8	18.1	167/26	169.7	18.9	6.7	-74.23	75.57	R
TE14a	171.8	8.2	167/26	174.9	5.3	8.2	-70.03	100.93	R
TE15	165.2	16.4	167/26	172.7	15.5	3.8	-74.24	88.40	R
TE16a	175.9	11.5	167/26	180.0	6.4	5.7	-71.21	116.00	R
TE21a	358.4	-13.2	167/26	3.0	-7.0	12.9	-71.29	125.37	N
TE22a	357.7	-14.1	167/26	2.8	-8.0	10.5	-71.82	124.98	N
TE23	2.5	-23.8	167/26	11.3	-14.8	5.0	-71.89	154.67	N
TE24	354.6	-17.2	167/26	1.4	-12.2	14.2	-74.11	121.09	N
TE25	351.0	-16.3	167/26	357.9	-12.8	6.5	-74.35	108.24	N
TE26a	2.9	-23.3	167/26	11.3	-14.2	8.6	-71.63	154.08	N
TE31	355.9	-15.7	167/33	3.0	-8.3	10.8	-71.94	125.69	N
TE32a	353.9	-15.4	167/33	1.2	-9.1	6.8	-72.54	119.99	N
TE33	0.4	-8.4	167/33	182.8	-0.1	7.0	-67.78	236.58	N
TE34	355.5	-7.5	167/33	358.2	-1.7	11.7	-68.78	111.02	N
TE35	358.8	-18.2	167/33	6.7	-9.0	7.6	-71.36	137.34	N

TE36a	355.9	-18.8	167/33	4.7	-11	8.1	-72.93	132.13	N
TE3X1	2.0	-17.0	164/34	179.8	-3.9	12.9	-66.05	244.49	N
TE3X2	2.3	-10.7	164/34	185.1	-1.0	7.2	-66.96	230.87	N
TE3x3a	354.5	-7.8	164/34	357.1	-0.7	6.5	-68.17	108.18	N
TE3X4	357.3	-7.0	164/34	178.9	-1.5	10.2	-67.22	246.84	N
TE3X5	359.5	-5.3	164/34	179.9	-4.1	3.3	-65.95	244.25	N
TE3x6a	8.9	-11.7	164/34	191.2	-3.5	5.7	-63.85	217.86	N
TE3X7	358.1	-15.0	164/34	4.0	-4.7	8.3	-69.97	127.74	N
TE41a	352.6	-17.2	168/39	2.5	-10.4	9.0	-73.07	124.58	N
TE42	344.0	-25.6	168/39	1.9	-22.0	7.3	-79.27	126.05	N
TE43	347.9	-11.3	168/39	355.1	-8.9	9.0	-71.85	100.14	N
TE44a	341.0	-12.2	168/39	350.4	-13.9	5.0	-72.42	82.78	N
TE45	0.2	-22.7	168/39	11.6	-10.2	4.0	-69.74	151.34	N
TE46	1.8	-23.8	168/39	13.5	-10.1	5.5	-68.63	155.65	N
TE48	3.4	-22.8	168/39	14.0	-8.4	7.0	-67.64	155.35	N
TE51a	347.6	-13.8	163/33	354.4	-9.0	9.7	-71.70	97.95	N
TE52	341.1	-10.9	163/33	347.4	-10.2	8.7	-69.19	78.29	N
TE53	343.2	-22.0	163/33	355.6	-18.2	3.6	-76.65	96.86	N
TE54	346.2	-6.3	163/33	349.1	-3.5	4.7	-67.14	86.88	N
TE55	343.6	-5.0	163/33	346.3	-3.9	5.8	-65.93	80.53	N
TE56a	342.1	-12.9	163/33	349.3	-11.3	5.2	-70.70	82.02	N
TE57	344.9	-6.4	163/33	348.1	-4.3	4.6	-67.03	84.13	N
TE61	157.6	21.5	166/36	172.6	22.1	4.6	-77.32	80.90	R
TE63a	152.3	15.1	166/36	164.1	20.2	5.8	-70.87	60.70	R
TE64	151.6	14.5	166/36	163.1	20.1	4.3	-70.06	59.00	R

TE65a	161.6	15.3	166/36	171.7	14.8	7.2	-73.46	85.82	R
TE71	333.8	-19.0	175/34	348.5	-27.5	7.1	-76.81	58.24	N
TE73	328.9	-21.5	175/34	345.9	-32.1	11.8	-75.96	42.58	N
TE74a	341.9	-19.9	175/34	355.9	-23.7	9.2	-79.61	93.21	N
TE75	346.6	-13.1	175/34	355.6	-15.5	8.3	-75.27	98.61	N
TE76	340.9	-16.6	175/34	352.9	-21.5	13.0	-77.19	82.83	N
TE77	329.9	-21.9	175/34	347.0	-32.0	7.6	-76.91	44.51	N
TE78	349.2	-3.9	175/34	352.4	-6.5	3.6	-69.86	93.45	N
TE79a	333.8	-19.7	175/34	348.9	-28.1	7.4	-77.34	57.95	N
TE81	349.9	-21.0	176/32	2.5	-20.9	7.9	-78.56	128.47	N
TE82a	348.1	-9.0	176/32	354.1	-11.8	11.8	-72.98	95.56	N
TE83	356.0	-15.9	176/32	4.6	-13.4	7.6	-74.16	132.96	N
TE84	357.3	-16.7	176/32	6.1	-13.4	5.0	-73.69	138.07	N
TE85a	358.3	-28.9	176/32	14.1	-23.1	7.8	-73.26	171.80	N
TE91a	189.6	14.9	169/29	194.0	3.4	13.6	-65.56	151.76	R
TE105	4.3	-24.3	170/34	195.3	12.4	8.6	-68.42	161.49	R
TE111	171.0	25.1	170/34	185.4	20.1	16.2	-77.27	140.84	R
TE116a	176.5	40.6	170/34	200.0	29.5	13.6	-70.11	191.30	R
TE121a	184.6	23.6	167/40	195.3	7.4	8.5	-66.45	157.23	R
TE123	182.5	17.6	167/40	190.0	3.9	8.4	-67.72	143.24	R
TE126	126.2	11.0	167/40	140.7	34.0	8.0	-53.09	23.94	R
TE131a	302.9	-8.7	168/39	135.3	33.9	8.7	-48.08	22.32	R
TE132	10.4	-11.3	168/39	12.6	4.8	8.7	-62.67	215.66	R
TE135	3.6	-5.6	168/39	3.7	5.3	8.1	-65.08	235.20	R
TE136	341.5	-17.4	168/39	174.3	17.5	7.7	-75.85	92.33	R

TE141	359.3	-28.1	174/38	16.0	-18.7	11.2	-70.27	169.61	N
TE142a	334.5	-47.4	174/38	17.3	-46.0	9.8	-73.41	311.63	N
TE143	341.5	-40.4	174/38	13.9	-37.8	5.2	-77.06	205.04	N
TE144a	312.8	-13.5	174/38	327.8	-35.4	10.0	-59.85	24.66	N
TE146	7.0	-48.9	174/38	36.2	-30.1	7.0	-55.38	202.75	N
TE148	350.0	-29.8	174/38	10.6	-25.4	3.6	-76.72	167.17	N
			Dec°	**Inc°**	**A95**	**k**	**n**		
Mean *in situ*			169.4	17.6	3.3	26.13	72		
Mean *with bedding correction*			179.4	14.0	3.5	23.73	72		

Sampling was performed across the succession, every specimen represented a single strata and thus, a time line. Following Deenen et al. (2011) each specimen was considered as an individual direction or in other words, a spot-readings of the geomagnetic field direction. Then, every direction features a VGP's. After applying a cut-off angle of 45° on the VGP's distribution, 72 were accepted from a total of 89 isolated directions (Fig. 10, Table 2). The discarded 17 directions were considered as outliers resulting from transitional data obtained during reversals.

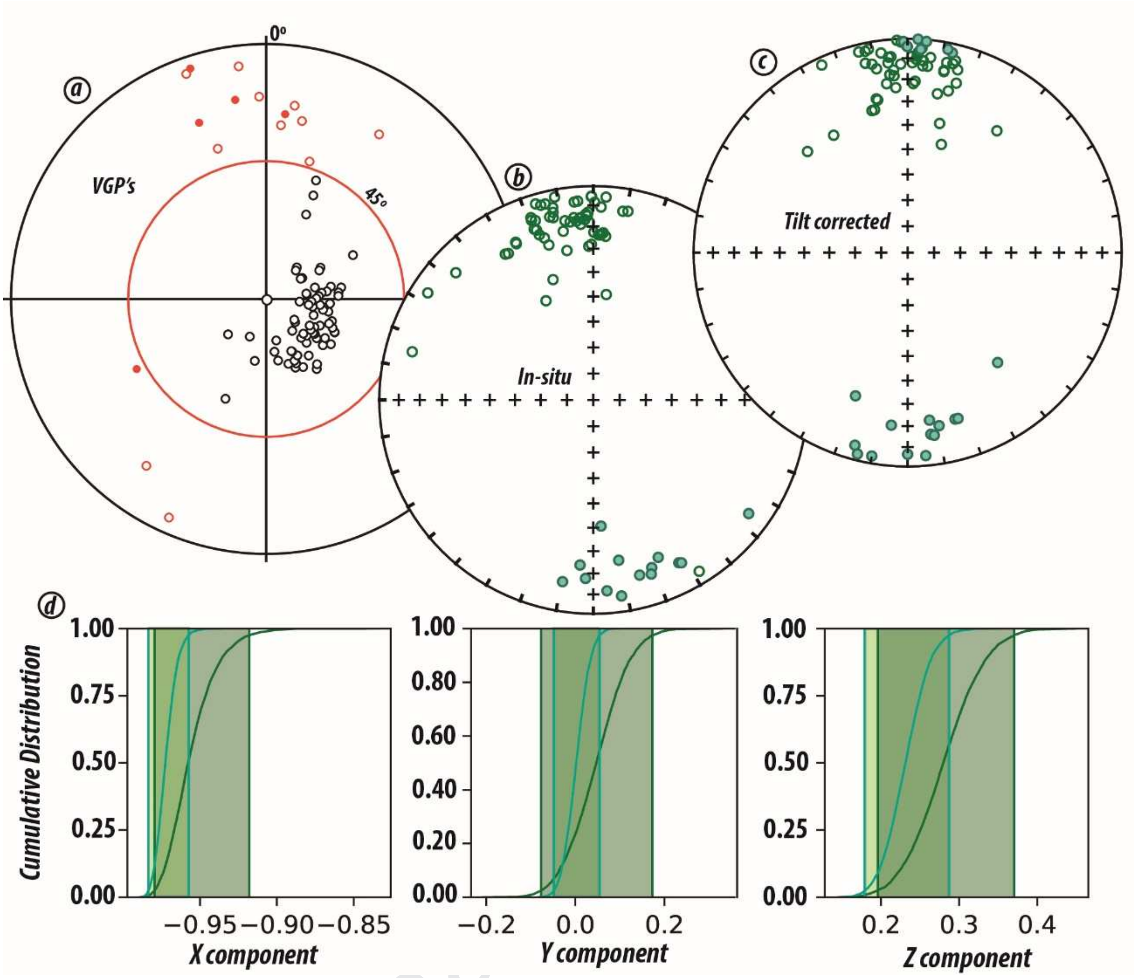

Figure 10. (a) Virtual geomagnetic poles (VGPs) distribution showing the fixed 45° cut-off angle. **(b)** Accepted ChRM directions in geographic coordinates. **(c)** Accepted tilt corrected ChRM directions. **(d)** Positive reversal test between both normal and reverse directions of ChRM, suggesting a primary magnetization of the studied rocks.

Reversal tests were performed to evaluate the antipodality of the mean direction of the normal and reverse populations. The data pass the bootstrap reversal test (Fig. 10d; Tauxe *et al.* 2010) as well as the McFadden and McElinnhy (McFadden and McElhinny, 1990) test classified as 'B' (Gamma= 5.2, critical Gamma= 9.39, R (95%)= 0.55), indicating that both populations are statistically equal.

Although a fold test could not be performed due to the logistical difficulty of sampling both flanks of the structure (Fig. 2), the magnetization is assumed to have been acquired before folding or during the initial stages of the deformation.

6 Quantifying vertical axis rotations: a bootstrap approach

The calculated paleomagnetic declination and inclination may be compared to values expected from paleomagnetic measurements from the stable part of the continent, the difference between measured and expected declination provides the tectonic rotation. In this contribution (Fig. 11), paleomagnetic directions were compared with the reference direction from the 20 Ma paleomagnetic pole of the global Apparent Polar Wander Path of Torsvik et al. (2012) in South American coordinates (Dec: 178.0, Inc: 45.6, $\alpha 95$: 2.6, following Torsvik et al., 2012) using the rotation parameter of Torsvik et al. (2012). Usually, tectonic rotations around a vertical axis are calculated with the method proposed by Demarest (1983) under the assumption that the directions follow a Fisher distribution (Fisher, 1953). However the distribution of paleomagnetic directions is elongated in N-S direction (e.g. Deenen et al., 2011; Tauxe and Kent, 2004). It is therefore inappropriate to use Fisher statistics in directional datasets (Tauxe and Kent, 2004). From this assumption, we have developed a nonparametric approach (e.g. Gallo et al., 2018) for the determination of tectonic rotations in a fully data-driven way where the uncertainties are calculated empirically, and based in the following bootstrap scheme:

1. Let $X = (X_1, \ldots, X_n)$ be the set of n observed directions where $X_i = (Dec_i, Inc_i)$. Let $X_{ref} = (Dec_{ref}, Inc_{ref})$ be the reference direction.

2. Calculate $\Delta R_i = Dec_i - Dec_{ref}$ and $\Delta I_i = Inc_i - Inc_{ref}$ for each of the n observed directions. Calculate ΔR_{mean} and ΔI_{mean} as the arithmetic means.
3. Obtain a pseudosample $X^* = (X_1, \ldots, X_n)$ of n observations by randomly drawing data (with replacement) from X. This procedure is repeated N_b times were $N_b >> n$. On each replicate ΔR_{mean} and ΔI_{mean} is computed against a new X_{ref} randomly draw direction from a Fisher distribution with the same mean direction and *k*; hence, we obtain $[\Delta R_{mean}^{(1)}, \ldots, \Delta R_{mean}^{(Nb)}]$ and $[\Delta I_{mean}^{(1)}, \ldots, \Delta I_{mean}^{(Nb)}]$.
4. ΔR and ΔI are calculated from the quantile 50% of the empirical distribution functions of $[\Delta R_{mean}^{(1)}, \ldots, \Delta R_{mean}^{(Nb)}]$ and $[\Delta I_{mean}^{(1)}, \ldots, \Delta I_{mean}^{(Nb)}]$, respectively.

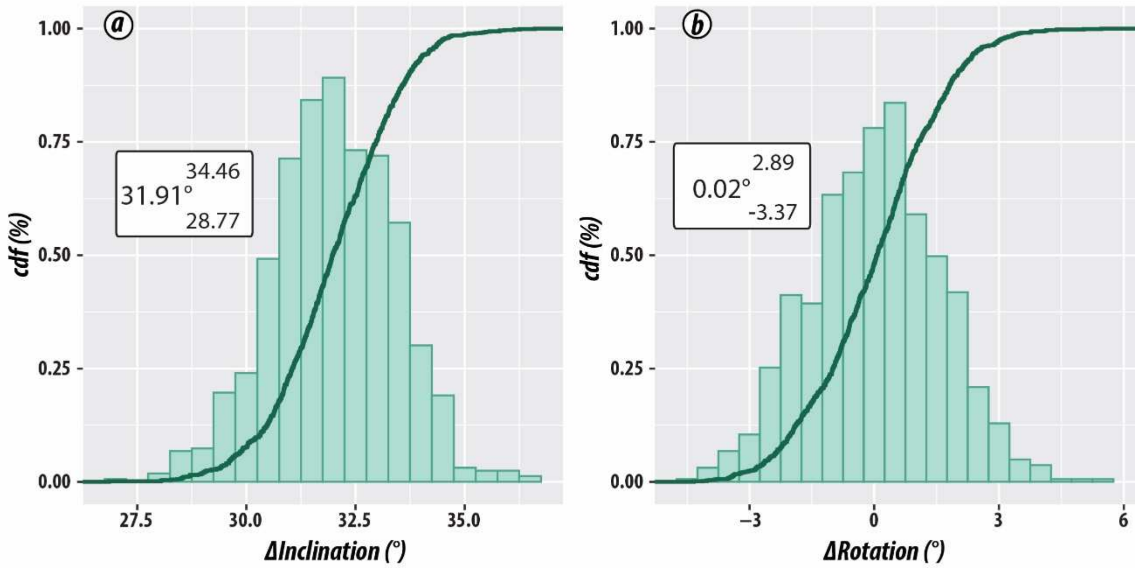

Figure 11. Vertical axis rotation results from the bootstrap procedure described in the text. The histograms show the frequency of the bootstrapped **(a)** ΔR and **(b)** ΔI. The variability of the parameters was used to estimate the 95% confidence bounds which lie between the 2.5 and 97.5% values of the empirical cumulative distribution functions

(green line).

From the above, we have obtained a $\Delta R=0.02°$ with an upper confidence bound of 2.9° and a lower bound of -3.4°. This parameter allows us to discard any statistically significant tectonic rotation of the studied area. The obtained $\Delta I=31.9°$ with upper and lower bounds of 34.5° and 28.8° respectively, and it is believed to be a bias due to compaction-induced inclination errors (further discussed in the next section).

7 Discussion

It is known that tectonic shortening is not enough to account for observed crustal thickness in the Central Andes (Baby et al., 1997; Kley and Monaldi, 1998). However, layer parallel shortening (LPS) can represent a significant component of the overall magnitude of shortening accommodated in an orogeny (e.g. Eichelberger and McQuarrie, 2014; Yonkee and Weil, 2010) and thus contributes in the total shortening budget. Moreover, LPS can also alters the kinematic path proposed in balanced cross-sections so that the material displacement parallel to the orogenic belt is addressed (e.g. Hindle et al., 2005). Thus, accounting for LPS in thrust sheets can alter the total shortening budget and the resulting kinematic model. Here, we have acquired fabric information by means of anisotropy of low-field magnetic anisotropy (AMS). AMS ellipsoid has been proven as an analog of preferred orientation of mineral grains and strain (see Borradaile, 2001; Rochette et al., 1992). The theoretical AMS fabric expected for sedimentary rocks is oblate, with the K_{min} axis in the vertical and perpendicular to the stratification plane, and with the K_{max} and K_{int} axes randomly arranged in a girdle contained within the stratification, (Tarling & Hrouda 1993, stage 'a' in Weil & Yonkee 2009). However, we show that the K_{max} axis (i.e. the maximum extension direction) although contained in the stratification plane, is not randomly distributed and it is not parallel to the structure (Az: 170º-350º). It tends to be grouped in the SSW-NNE quadrant (Fig. 7). This suggests that there is a preferred orientation of present magnetic grains (Stage "b" of Weil & Yonkee 2009) indicating a WNW-ESE direction of maximum shortening, parallel to the layers in the horizontal position before the folding (first stage of the deformation; Fig. 12 a). This implies the presence of material displacements parallel to the orogenic trend (roughly N-S, Fig. 4). The regional stress field was controlled by a principal stress from the W-NW (Fig. 12). At the time of folding, the internal structure of the rocks was already being acquired (Fig. 12 a) and prior to the folding, occurred the development of joints (Fig. 12 b. and Fig. 4) and the subsequent folding that leads the layers to their present attitude (SSE-NNW). For this stage, the field of local efforts acquires an abnormal ENE-WSW direction, respect to the southern regional Subandean trends structure (Fig. 4 and 12 c).

The studied rocks have a characteristic remanent magnetization with normal and reverse polarity, consistent with a primary magnetization acquired during the Miocene and before the folding of the sequence. This observation is supported by a high-field coercitivity spectra and blocking temperatures up to 680º (stable magnetization carried by hematite), that we interpret the carriers of the magnetization as hematite and/or titano-hematite. The characteristic directions isolated by PCA indicate a single high-blocking temperature component. The samples were taken from a 60 meters succession (see Fig. 3) where we found normal and reverse polarity zones, implying that the secular variation was properly averaged.

After applying a cut-off angle of 45º on the VGP's distribution, 72 from a total of 89 isolated directions were accepted (Fig. 11, Table 2) and subsequently used for the directional analysis. The mean direction based on these accepted specimens (n = 72) was *in situ*: Dec = 169.4 °, Inc = 17.6 °, k = 26.1, $\alpha95$ = 3.3º. After full bedding correction the mean direction is: Dec = 179.4°, Inc = 14º, k = 23.73, $\alpha95$ = 3.5º (Fig. 13).

If the inclination shallowing correction envisaged by Tauxe and Kent (2004) is applied to the corrected mean directions, the distribution of VGP's produces a distribution related to a flattening factor f=0.62. The corrected inclination is 20.37º with bootstrapped confidence bounds of 14.77º to 25.28º, and an elongation parameter of 2.5.

It is important to note that this correction necessitates at least 100 spot-readings of the geomagnetic field, a number greater than the existing samples, and thus, we consider the obtained correction as an approximation rather than the real flattening factor. The directions pass a reversal test allowing us to assume that the magnetization is likely to be primary. Based on the accepted directions, a paleomagnetic pole (PP) was calculated for the Miocene Tariquia Formation: Lat. = 78.4º S, Long. = 113.1º E, A95= 3.5º (Fig. 13).

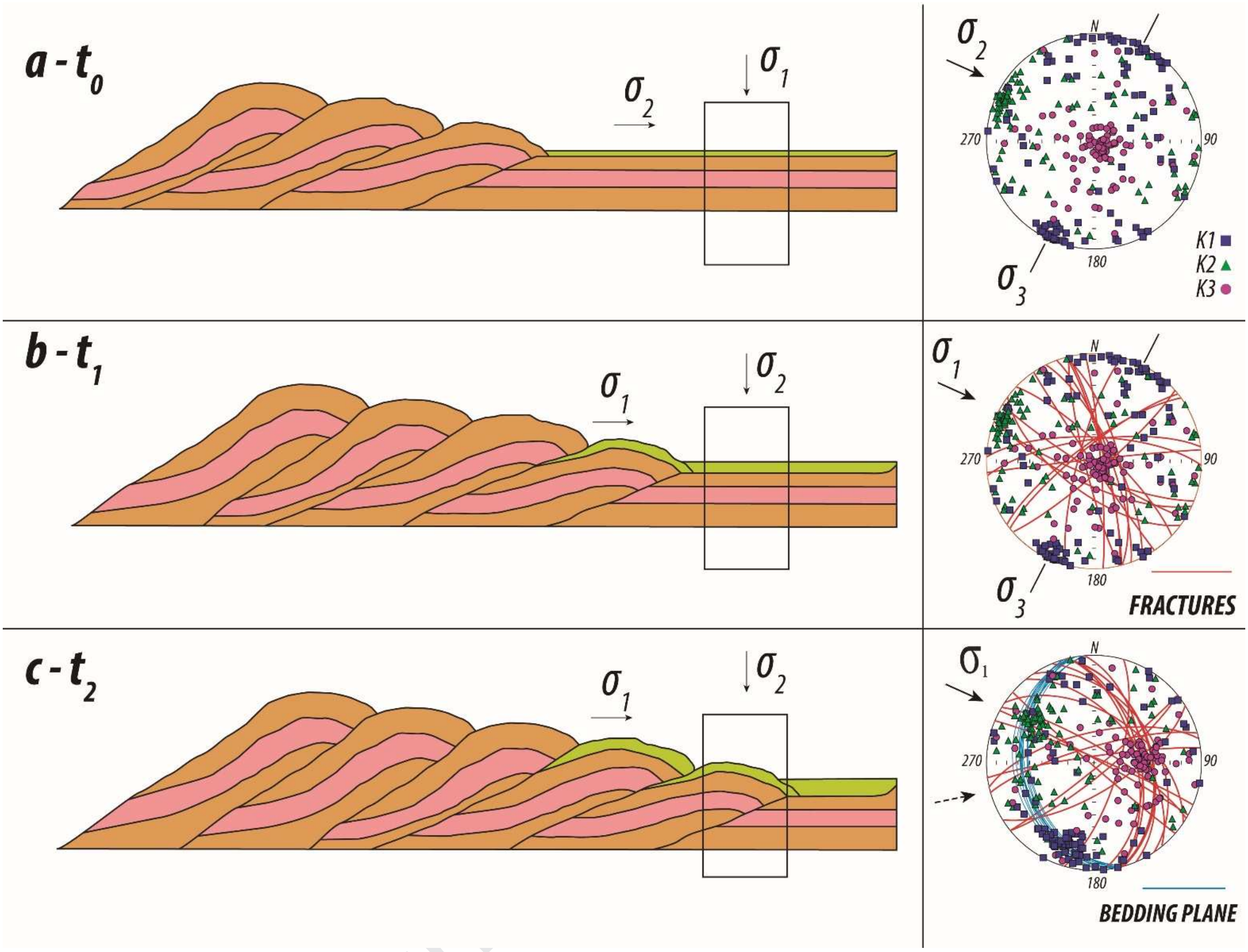

Figure 12. Model of the structural evolution. The rectangle represents the sampled zone. In yellow: Miocene Tariquia Formation. **(a)** the principal stress σ1 is perpendicular to the bedding plane, responding to a maximum stress corresponding to the sedimentary load, and σ2 represents the regional applied stress that occurs in the west, with WNW-ESE direction. At this time the AMS is being acquired. **(b)** with the deformation front approaching from the west, the σ1 being located in a WNW-ESE position and the σ2 occupied the vertical position perpendicular to the bedding plane. At the first stage of deformation, the formation of joints takes place. For this time, the rocks magnetic fabric had already been acquired. **(c)** in this stage occurs the folding with a regional σ1 in a position WNW-ESE, but with local stress (dotted arrow) rotated respect of the regional σ1 as a consequence of anisotropy in the basement giving an anomalous structure with NNW-SSE strike.

From the scalar analysis of the AMS parameters, differences arise between samples from the base with those of the top of the sequence. The anisotropy degree (P_j)even when it is less than 19% in the entirety of the sedimentary package, increases towards the base. The shape parameter T also changes from oblate to the base to prolate-towards the top (Table 1; Fig. 8). No strong functional relationship between anisotropy degree or shape parameter (Fig. 8d and 8e) and magnetic susceptibility was seen, implying that the scalar parameters of AMS are mainly controlled by the stratigraphic position (i.e. increasing Pj and T towards the base due to compaction). Thus, we interpret that the sedimentary column has been subjected to heavy compaction processes. It is argued that the obtained paleomagnetic pole of reference owing to a shallowing in the paleomagnetic inclination.

It was ruled out the possibility of rotations about vertical axes as is usually thought from paleomagnetic around the Arica bend. From a newly developed nonparametric approach to quantify vertical axis rotations, we found that there are no significant statistical differences in the declination between the reference pole for the Miocene (Torsvik et al., 2012) and the obtained data (Fig. 13). The local change in the azimuth of the structures, while the paleomagnetic data do not show rotation, could be the consequence of a previous basement structure, basement heterogeneity (thickness or rheological variations), and/or even be the consequence of exogenous agents (Darnault et al., 2016) as there could be differences in erosion along the course of the structures, or the combination of these factors.

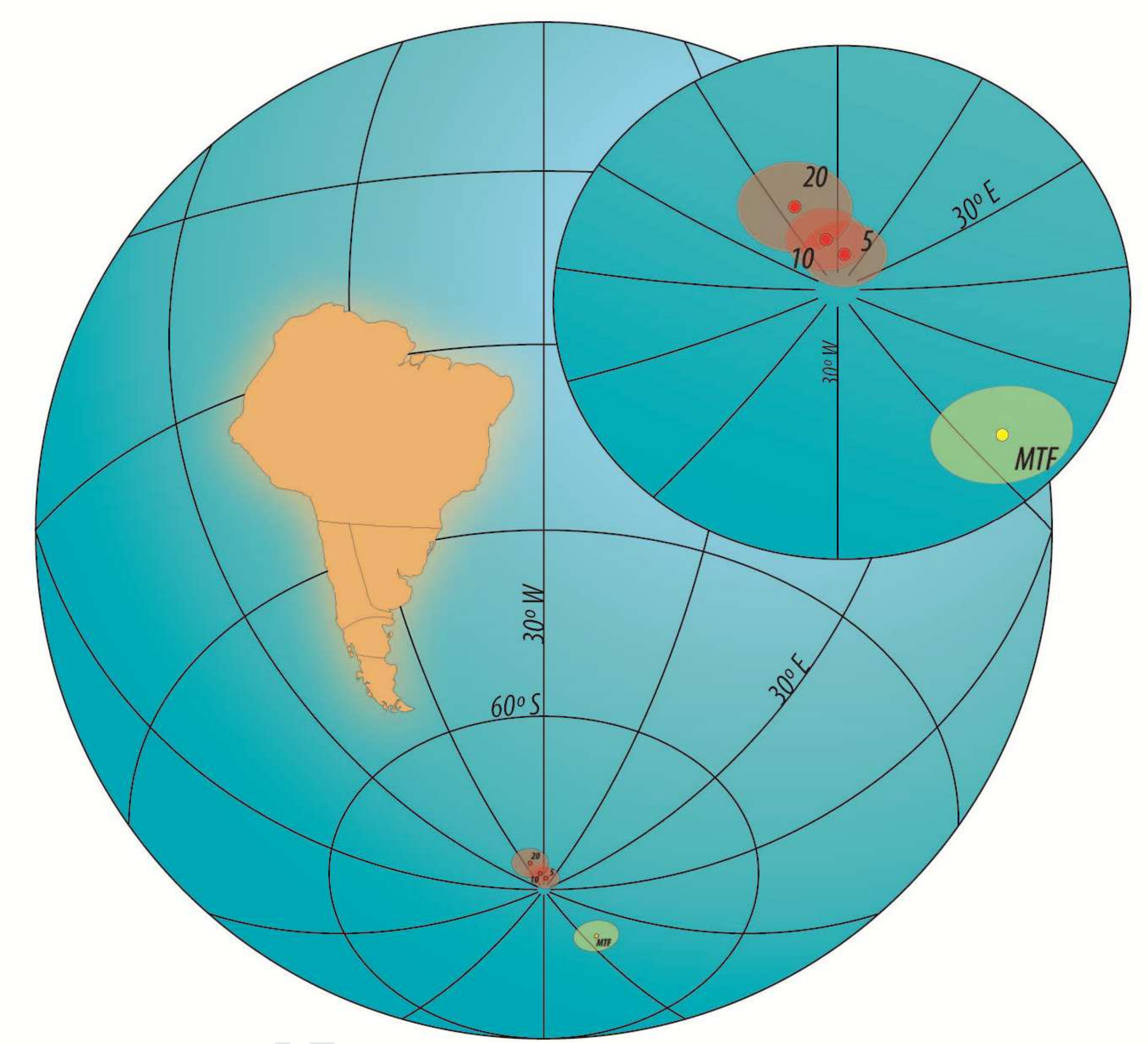

Figure 13. Paleomagnetic pole with A95 in South American coordinates from obtained data. Yellow dot: Miocene Tariquia Formation pole (MTF; Lat.= 78.4º S, Long.= 113.1º E, A95=3.5º). Red dots: poles of 5, 10 and 20 Ma (from Torsvik *et al.* 2012).

8 Conclusions

Unraveling the complex three-dimensional kinematic history of the Bolivian orocline necessitates reporting for material displacements parallel to the trend of the orogen and vertical axis rotations. Here, we address strain and shortening direction as well as layer parallel shortening (LPS) by means of new paleomagnetic and AMS data. On the one hand, the paleomagnetic study reveals the absence of vertical axis rotations in the studied area. The magnetization is likely to be acquired before the deformation, probably during the deposition of the sediments. This is consistent with the presence of normal and reversed polarities in the same succession, which yields a positive reversal test. The Miocene Tariquia Formation paleomagnetic pole obtained is: Lat. = 78.4º S, Long = 113.1º E, A95= 3.5º.

On the other hand, the study of AMS reveals that the fabric must have been acquired before folding (i.e. pre-tectonic fabric) and during the initials stages of LPS. This implies that the magnetic lineation (i.e. the maximum extension direction) has been perpendicular to the maximum regional stress before folding. However, the structural trend is not parallel to the magnetic lineation (i.e. shortening direction not perpendicular to the bedding planes). This also implies material displacement parallel to the orogenic belt, and this is not resolved in balanced cross sections performed perpendicularly to the orogenic trend. Thus, it is proposed that during the development of faulting and folding at this latitude, externals factors (i.e. structural anisotropies within the basement) could have conditioned the trend and growth of the structure without the need of rotations around a vertical axis. Finally, LPS can represent a significant component of the overall magnitude of shortening (e.g. Eichelberger and McQuarrie, 2014) and can also alter the kinematic path proposed in balanced cross-sections. Thus, we stress the need for accounting for LPS and shortening direction while performing balanced cross sections, and we highlight AMS studies as a means for doing so.

Acknowledgments

The field work was possible with the logistical support of XR-Geomap. All measures were made at the "Daniel A. Valencio" Laboratory, Facultad de Ciencias Exactas y Naturales, Universidad de Buenos Aires. This work was funding through the Vinculación Tecnológica "Jorge A. Sábato", "Agregando Valor" projects. We thank comments and suggestions from Fernando Poblete and Roman Veselovskiy that improve significantly the manuscript.

References

Allmendinger, R.W., Smalley, R., Bevis, M., Caprio, H., Brooks, B., Sciences, A., York, N., Smalley, R., Bevis, M., Caprio, H., Brooks, B., 2005. Bending the Bolivian orocline in real time. Geology 33, 905. https://doi.org/10.1130/G21779.1

Arriagada, C., Roperch, P., Mpodozis, C., Cobbold, P.R., 2008. Paleogene building of the Bolivian Orocline: Tectonic restoration of the central Andes in 2-D map view. Tectonics 27, n/a-n/a. https://doi.org/10.1029/2008TC002269

Arriagada, C., Roperch, P., Mpodozis, C., Fernandez, R., 2006. Paleomagnetism and tectonics of the southern Atacama Desert (25-28°S), northern Chile. Tectonics 25, n/a-n/a. https://doi.org/10.1029/2005TC001923

Baby, P., Rochat, P., Mascle, G., Herail, G., 1997. Neogene shortening contribution to crustal thickening in the back arc of the Central Andes. Geology 25, 883–886. https://doi.org/10.1130/0091-7613(1997)025<0883:NSCTCT>2.3.CO;2

Barke, R., Lamb, S., MacNiocaill, C., 2007. Late Cenozoic bending of the Bolivian

Andes: New paleomagnetic and kinematic constraints. J. Geophys. Res. 112, B01101. https://doi.org/10.1029/2006JB004372

Belotti, H.J., Saccavino, L.L., Schachner, G.A., 1995. Structural Styles and Petroleum Occurrence in the Sub-Andean Fold and Thrust Belt of Northern Argentina, in: Tankard, A.J., Suárez Soruco, R., Welsink, H.J. (Eds.), Petroleum Basins of South America. AAPG Special Volumes, pp. 545–555.

Borradaile, G.J., 2001. Magnetic fabrics and petrofabrics: their orientation distributions and anisotropies. J. Struct. Geol. 23, 1581–1596. https://doi.org/10.1016/S0191-8141(01)00019-0

Brooks, B. a., Bevis, M., Whipple, K., Ramon Arrowsmith, J., Foster, J., Zapata, T., Kendrick, E., Minaya, E., Echalar, A., Blanco, M., Euillades, P., Sandoval, M., Smalley, R.J., 2011. Orogenic-wedge deformation and potential for great earthquakes in the central Andean backarc. Nat. Geosci. 4, 380–383. https://doi.org/10.1038/ngeo1143

Calle, A.Z., Horton, B.K., Limachi, R., Stockli, D.F., Anderson, R.B., Long, S.P., 2018. Cenozoic Provenance and Depositional Record of the Sub-Andean Foreland Basin during Growth of the Central Andean Fold-Thrust Belt, Southern Bolivia 475–522. https://doi.org/10.1306/13622132m1173777

Carey, S.W., 1955. The Orocline Concept in Geotectonics Part I. R. Soc. Tasmania Pap. Proc. 89, 255–288.

Darnault, R., Callot, J.P., Ballard, J.F., Fraisse, G., Mengus, J.M., Ringenbach, J.C., 2016. Control of syntectonic erosion and sedimentation on kinematic evolution of a multidecollement fold and thrust zone: Analogue modeling of folding in the southern subandean of Bolivia. J. Struct. Geol.

https://doi.org/10.1016/j.jsg.2016.05.009

Deenen, Martijn H.L., Langereis, C.G., van Hinsbergen, D.J.J., Biggin, A.J., 2011. Geomagnetic secular variation and the statistics of palaeomagnetic directions. Geophys. J. Int. 186, 509–520. https://doi.org/10.1111/j.1365-246X.2011.05050.x

Deenen, Martijn H L, Langereis, C.G., van Hinsbergen, D.J.J., Biggin, A.J., 2011. Geomagnetic secular variation and the statistics of palaeomagnetic directions. Geophys. J. Int. 186, 509–520. https://doi.org/10.1111/j.1365-246X.2011.05050.x

Demarest, H.H., 1983. Error analysis for the determination of tectonic rotation from paleomagnetic data. J. Geophys. Res. Solid Earth 88, 4321–4328. https://doi.org/10.1029/JB088iB05p04321

Dunlop, D.J., Özdemir, O., 1997. Rock magnetism : fundamentals and frontiers. Cambridge University Press.

Eichelberger, N., McQuarrie, N., 2014. Three-dimensional (3-D) finite strain at the central Andean orocline and implications for grain-scale shortening in orogens. Geol. Soc. Am. Bull. 87–112. https://doi.org/10.1130/B30968.1

Eichelberger, N., McQuarrie, N., Ehlers, T. a., Enkelmann, E., Barnes, J.B., Lease, R.O., 2013. New constraints on the chronology, magnitude, and distribution of deformation within the central Andean orocline. Tectonics 32, 1432–1453. https://doi.org/10.1002/tect.20073

Fisher, R., 1953. Dispersion on a Sphere. Proc. R. Soc. A Math. Phys. Eng. Sci. 217, 295–305. https://doi.org/10.1098/rspa.1953.0064

Gallo, L.C.L.C., Cristallini, E.O.E.O., Svarc, M., 2018. A Nonparametric Approach for Assessing Precision in Georeferenced Point Clouds Best Fit Planes: Toward More

Reliable Thresholds. J. Geophys. Res. Solid Earth 123, 10,297-10,308. https://doi.org/10.1029/2018JB016319

Hindle, D., Kley, J., Oncken, O., Sobolev, S., 2005. Crustal balance and crustal flux from shortening estimates in the Central Andes. Earth Planet. Sci. Lett. 230, 113–124. https://doi.org/10.1016/j.epsl.2004.11.004

Hrouda, F., Jelínek, V., Zapletal, K., 1997. Refined technique for susceptibility resolution into ferromagnetic and paramagnetic components based on susceptibility temperature-variation measurement. Geophys. J. Int. 129, 715–719. https://doi.org/10.1111/j.1365-246X.1997.tb04506.x

Isacks, B.L., 1988. Uplift of the Central Andean Plateau and bending of the Bolivian Orocline. J. Geophys. Res. 93, 3211. https://doi.org/10.1029/JB093iB04p03211

Jelinek, V., 1981. Characterization of the magnetic fabric of rocks. Tectonophysics. https://doi.org/10.1016/0040-1951(81)90110-4

Kirschvink, J.L., 1980. The least-square line and plane and the analysis of paleomagnetic data. Geophys. J. R. Astron. Soc. 62, 699–718.

Kley, J., 1996. Transition from basement-involved to thin-skinned thrusting in the Cordillera Oriental of southern Bolivia. Tectonics 15, 763–775. https://doi.org/10.1029/95TC03868

Kley, J., Monaldi, C.R., 1998. Tectonic shortening and crustal thickness in the Central Andes: How good is the correlation-? Geology 26, 723–726. https://doi.org/10.1130/0091-7613(1998)026<0723:TSACTI>2.3.CO;2

Lease, R.O., Ehlers, T.A., Enkelmann, E., 2016. Large along-strike variations in the onset of Subandean exhumation: Implications for Central Andean orogenic growth.

Earth Planet. Sci. Lett. 451, 62–76. https://doi.org/10.1016/j.epsl.2016.07.004

Maxbauer, D.P., Feinberg, J.M., Fox, D.L., 2016. MAX UnMix: A web application for unmixing magnetic coercivity distributions. Comput. Geosci. 95, 140–145. https://doi.org/10.1016/J.CAGEO.2016.07.009

McFadden, P.L., McElhinny, M.W., 1990. Classification of the reversals test in palaeomagnetism. Geophys. J. Int. 103, 725–729. https://doi.org/10.1111/j.1365-246X.1990.tb05683.x

McQuarrie, N., 2002. The kinematic history of the central Andean fold-thrust belt, Bolivia: Implications for building a high plateau. Bull. Geol. Soc. Am. 114, 950–963. https://doi.org/10.1130/0016-7606(2002)114<0950:TKHOTC>2.0.CO;2

McQuarrie, N., Barnes, J.B., Ehlers, T.A., 2008. Geometric, kinematic, and erosional history of the central Andean Plateau, Bolivia (15-17°S). Tectonics 27. https://doi.org/10.1029/2006TC002054

Rochette, P., Jackson, M., Aubourg, C., 1992. Rock magnetism and the interpretation of anisotropy of magnetic susceptibility. Rev. Geophys. 30, 209. https://doi.org/10.1029/92RG00733

Roperch, P., Sempere, T., Macedo, O., Arriagada, C., Fornari, M., Tapia, C., García, M., Laj, C., 2006. Counterclockwise rotation of late Eocene-Oligocene fore-arc deposits in southern Peru and its significance for oroclinal bending in the central Andes. Tectonics 25, n/a-n/a. https://doi.org/10.1029/2005TC001882

Somoza, R., Tomlinson, a. J., Zaffarana, C.B., Singer, S.E., Puigdomenech Negre, C.G., Raposo, M.I.B., Dilles, J.H., 2015. Tectonic rotations and internal structure of Eocene plutons in Chuquicamata, northern Chile. Tectonophysics 654, 113–130.

https://doi.org/10.1016/j.tecto.2015.05.005

Somoza, R., Tomlinson, A., 2002. Paleomagnetism in the Precordillera of northern Chile (22°30’S): Implications for the history of tectonic rotations in the Central Andes. Earth Planet. Sci. Lett. 194, 369–381. https://doi.org/10.1016/S0012-821X(01)00548-9

Somoza, R., Zaffarana, C.B., 2008. Mid-Cretaceous polar standstill of South America, motion of the Atlantic hotspots and the birth of the Andean cordillera. Earth Planet. Sci. Lett. 271, 267–277. https://doi.org/10.1016/j.epsl.2008.04.004

Somoza, Singer, S., Coira, B., 1996. Paleomagnetism of upper Miocene ignimbrites at the Puna: An analysis of vertical-axis rotations in the Central Andes. J. Geophys. Res. 101, 11387–11400. https://doi.org/10.1029/95jb03467

Sprain, C.J., Feinberg, J.M., Renne, P.R., Jackson, M., 2016. Importance of titanohematite in detrital remanent magnetizations of strata spanning the Cretaceous-Paleogene boundary, Hell Creek region, Montana. Geochemistry, Geophys. Geosystems 17, 660–678. https://doi.org/10.1002/2015GC006191

Tarling, D.H. (Donald H., Hrouda, F. (František), 1993. The magnetic anisotropy of rocks. Chapman & Hall.

Tauxe, L., Butler, R.F., Van der Voo, R. (Rob), Banerjee, S.K., 2010. Essentials of paleomagnetism. University of California Press.

Tauxe, L., Kent, D., 2004. A simplified statistical model for the geomagnetic field and the detection of shallow bias in paleomagnetic inclinations: Was the ancient magnetic field dipolar. Timescales Paleomagn. Field, 145, 101–115. https://doi.org/10.1029/145GM08

Torsvik, T.H., Van der Voo, R., Preeden, U., Niocaill, C. Mac, Steinberger, B., Doubrovine, P. V., van Hinsbergen, D.J.J., Domeier, M., Gaina, C., Tohver, E., Meert, J.G., McCausland, P.J.A., Cocks, L.R.M., 2012. Phanerozoic polar wander, palaeogeography and dynamics. Earth-Science Rev. 114, 325–368. https://doi.org/10.1016/j.earscirev.2012.06.002

Uba, C.E., Heubeck, C., Hulka, C., 2005. Facies analysis and basin architecture of the Neogene Subandean synorogenic wedge, southern Bolivia. Sediment. Geol. 180, 91–123. https://doi.org/10.1016/j.sedgeo.2005.06.013

Uba, C.E., Kley, J., Strecker, M.R., Schmitt, A.K., 2009. Unsteady evolution of the Bolivian Subandean thrust belt: The role of enhanced erosion and clastic wedge progradation. Earth Planet. Sci. Lett. 281, 134–146. https://doi.org/10.1016/J.EPSL.2009.02.010

Valet, J., Meynadier, L., Simon, Q., Thouveny, N., 2016. When and why sediments fail to record the geomagnetic field during polarity reversals. Earth Planet. Sci. Lett. 453, 96–107. https://doi.org/10.1016/j.epsl.2016.07.055

Weil, A.B., Sussman, A.J., 2004. Classifying curved orogens based on timing relationships between structural development and vertical-axis rotations. Spec. Pap. Geol. Soc. Am. 383, 1–15. https://doi.org/10.1130/0-8137-2383-3(2004)383[1:CCOBOT]2.0.CO;2

Weil, A.B., Yonkee, A., 2009. Anisotropy of magnetic susceptibility in weakly deformed red beds from the Wyoming salient, Sevier thrust belt: Relations to layer-parallel shortening and orogenic curvature. Lithosphere 1, 235–256. https://doi.org/10.1130/L42.1

Weil, A.B., Yonkee, A., Sussman, A., 2010. Reconstructing the kinematic evolution of curved mountain belts: A paleomagnetic study of Triassic red beds from the Wyoming salient, Sevier thrust belt, U.S.A. Bull. Geol. Soc. Am. 122, 3–23. https://doi.org/10.1130/B26483.1

Yonkee, A., Weil, A.B., 2010. Reconstructing the kinematic evolution of curved mountain belts : Internal Reconstructing the kinematic evolution of curved mountain belts : Internal strain patterns in the Wyoming salient , Sevier thrust belt , U . S . A . https://doi.org/10.1130/B26484.1

Zijderveld, A.C., 1967. Demagnetization of rocks: Analysis of results, in: Methods in Palaeomagnetism, ed. D. W. Collinson, K. M. Creer, and S. K. Runcorn, Elsevier, 254-286.

HIGHLIGHTS

- Absence of vertical axis rotation in the southern Subandes of Bolivia
- Nonparametric approach to quantify vertical axis rotations
- New Miocene paleomagnetic data of the southern Subandes of Bolivia

Author Statement

- **Mr. Juan Martín Calvagno:** Conceptualization, Methodology, Software, Formal analysis, Investigation, Writing – Original Draft, Writing Review and editing, Visualization, Supervision
- **Dr. Leandro C. Gallo:** Conceptualization, Methodology, Software, Formal analysis, Investigation, Writing – Original Draft, Writing Review and editing, Visualization
- **Dra. Renata N. Tomezzoli:** Conceptualization, Methodology, Investigation, Writing – Original Draft, Project Administration, Resources
- **Dr. Ernesto O. Cristallini:** Conceptualization, Resources
- **Dra. Alejandra Dalenz Farjat:** Validation
- **Mr. Roberto M. Hernández:** Validation, Resources

Declaration of interests

☒ The authors declare that they have no known competing financial interests or personal relationships that could have appeared to influence the work reported in this paper.

☐The authors declare the following financial interests/personal relationships which may be considered as potential competing interests: